2026 IEEE International Conference on Robotics and Automation (ICRA 2026)
June 1-5, 2026. Vienna, Austria

Design and Dynamic Modeling of a Flying Fish Robot with Experimental Validation

Jiayi Jin[1] and Wei Wang[1,*]

***Abstract*— Flying fish have often served as an inspiration for engineering designs due to their remarkable ability for cross-domain locomotion between water and air. Previous observations and simulations suggest that taxiing behavior before takeoff is indispensable, yet the mechanics of this transition remain unclear. In this work, we present the design and dynamic modeling of a robotic flying fish to investigate swimming and taxiing locomotion, with a particular focus on tail pitching. We develop a bio-inspired prototype with an active tail-pitching structure and a high-power-density tail-beating propulsion system. We further formulate a cross-domain dynamic model that couples hydrodynamic and aerodynamic forces during taxiing. Simulations show that pitching the tail downward increases peak height and enables the robot to leave the water at a more aerodynamically favorable angle of attack. Experiments with the robotic prototype validate these trends and show that downward tail pitching increases upward force and body elevation with only minor loss of forward speed. These results provide insight into the role of tail pitching in flying fish taxiing and takeoff preparation.**

***Index Terms*—Marine Robotics, Biologically-Inspired Robots, Simulation and Animation, Robot Dynamics**

I. Introduction

Aerial-aquatic locomotion is the seamless transition between swimming and flight in water and air. Some animals, like gannets, guillemots, flying squids, and flying fish, excel at this [1]. Flying fish (*Exocoetidae*) are unique fish that rapidly switch between air and water locomotion. They swim underwater, taxi along the surface, and glide in the air [2]. Underwater swimming relies on the caudal fin for thrust. The fish approaches the surface at high speed, breaks through, deploys the pectoral fins and enters taxiing mode. In taxiing mode, the caudal fin beats at high frequency while most of the body is above the water, until it takes off and glides [3].

Flying fish's unique cross-domain locomotion has captivated researchers developing aquatic-aerial robots. However, close study is challenging due to complex high-frequency kinematics and dynamics, a wide operation range, and limited habitat [2]. Early work qualitatively described locomotion modes based on field observations but lacked details and principles [2]–[4]. To overcome data collection challenges [5], researchers used lab and numerical methods for quantitative analysis. Park and Choi [6] studied aerodynamic properties of preserved flying fish in a wind tunnel, measuring lift, drag, and pitching moment coefficients. Deng et al. [7] numerically studied aerodynamics using computational fluid dynamics, visualizing the flow field in detail.

[1]Marine Robotics Lab, Department of Mechanical Engineering, University of Wisconsin–Madison, Madison, WI 53706, USA.
[*]Corresponding author: Wei Wang (e-mail: wwang745@wisc.edu).

In addition to field or lab experiments, robotic models have been used to study flying fish, expanding experimental space by modifying designs, which is not possible with animal specimens [8]. Gao and Techet [9] proposed a passive model and discussed conceptual designs of actuation and control. Saro-Cortes [10] et al. designed a passive model to investigate the pelvic fin's aerodynamic role in gliding. Active systems include Kawachi et al.'s analysis of the ideal gliding path using optimal control [11] and Chen et al.'s robotic flying fish with morphing pectoral fins that improve gliding distance through optimization control [12]. These robots nevertheless remain distant from real flying fish, particularly in terms of taxiing and takeoff capabilities.

While most recent studies focused on the flying locomotion of the flying fish, the other two locomotion modes, swimming and taxiing, have been less studied. Flying fish have been seen to taxi on the water surface by rapidly beating their semi-submerged tails (Fig. 1(a)). Deng et al. [13] revealed the benefits and significance of taxiing through numerical simulations. Their results showed that taxiing helps transition because it allows the flying fish to further accelerate to a higher takeoff speed on the water surface at substantially lower hydrodynamic resistance, which may help the flying fish to glide over a longer distance [2]. During taxiing, it has been observed that the tail is pitched downwards, submerging the lower lobe of the caudal fin [14]. Since tail pitching is a distinctive kinematic feature observed during taxiing, investigating its role is important for understanding taxiing mechanics. However, the underlying mechanism by which pitching the tail downwards aids flying fish in takeoff and the associated strategies remain unclear.

In this paper, we investigate the taxiing locomotion of flying fish using a robotic platform, with a particular focus on the role of tail pitching. We developed a robotic flying fish prototype equipped with a powerful fish-like propulsion system and an active tail-pitching mechanism. We further established a novel cross-domain dynamic model that integrates hydrodynamics and aerodynamics to analyze how tail pitching influences taxiing performance. The main contributions of our work are:

1) A robotic flying fish prototype with an actively adjustable tail-pitching mechanism for studying taxiing locomotion.
2) A cross-domain self-propelled dynamic model of flying fish taxiing, coupling hydrodynamic and aerodynamic forces on the partially submerged body.
3) Simulation and experimental results revealing the impact of tail pitching on the taxiing performance.

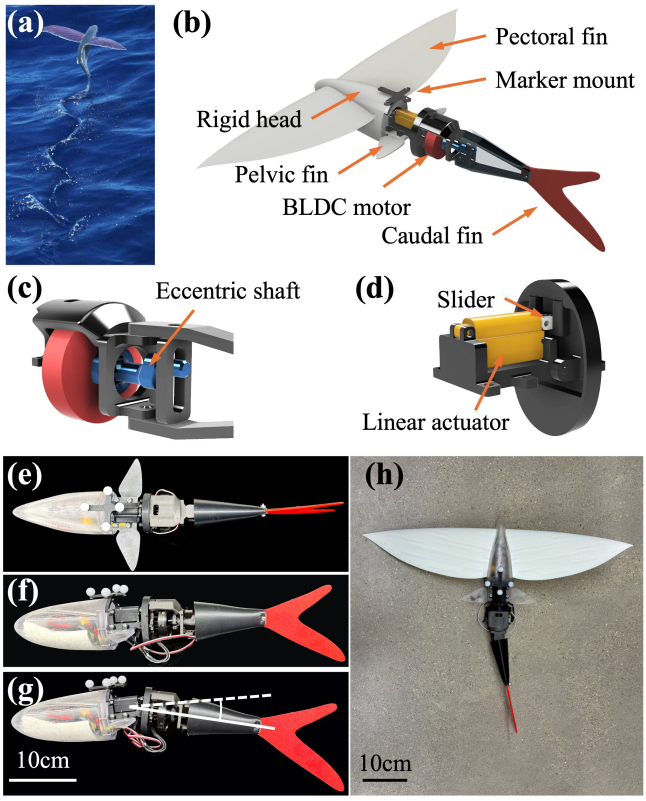

Fig. 1. (a) A flying fish taking off after taxiing on the water surface. *Credit: The NOAA Marine Operations Center*. (b) Design of the robotic flying fish. The robotic flying fish consists of a streamlined rigid head, a tail-pitching structure, a self-propelled tail, a pair of pectoral fins, a pair of pelvic fins, and a caudal fin. (c) Design of the transmission structure that converts the continuous rotation of the BLDC motor into a tail beating motion. (d) Design of the tail-pitching structure. (e, f) The top view (e) and side view (f) of the robotic flying without the pectoral fins mounted. (g) The tail-pitching structure caused a downward pitch of the tail by $10°$. (h) The top view of the robotic fish with the pectoral fins mounted.

II. Design of Robotic Flying Fish

For the purpose of realizing high performance in speed, the robotic flying fish was deliberately developed in many aspects. As illustrated in Fig. 1(b), the robotic flying fish consists of a self-propelled robotic fish and a pair of wing-like pectoral fins.

The pectoral fin outlines are derived from [7]. A low-profile airfoil, SD7037, is selected as the chordwise cross-section to reduce thickness. The designed pair of pectoral fins has a chord length of 110 mm, a span of 598 mm, and an aspect ratio of 8.1. A $15°$ lateral dihedral angle is applied when the pectoral fins are attached to the head, which has been experimentally validated to enhance the lateral and longitudinal static stability [6], [15].

The robotic fish comprises a rigid head, a tail-pitching structure, a pair of pelvic fins, and a self-propelled tail with a caudal fin. The rigid head replicates the shape of an animal flying fish [6]. The flat-bottomed nature of the fish body has been captured in the shape design, which has been implicated in yielding extra lift [3]. The rigid head is a streamlined shell with a thickness of 1 mm, designed to securely hold electronic components. The waterproofing is achieved through a specially designed sealing structure at the cap and a cable gland. Moreover, two reflective markers are mounted on the top to measure the velocity and pitching angle of the robotic fish.

As previously indicated, the propulsion system requires a high power density. Compared with conventional electromagnetic direct current motors, brushless direct current (BLDC) motors offer more powerful output with a more compact structure and lighter weight. Moreover, BLDC motors, free from the rotor-stator contact as in other DC motors, require minimal waterproofing treatment, further simplifying the design. A high-torque, high-energy-density BLDC motor (MN5008 Antigravity 170KV, T-MOTOR) is employed as the actuator of the robotic fish. The motor was selected to balance speed, torque output, and compact size. Notably, it can directly drive the tail without the need for modifying the motor or integrating a gearbox, as previously applied in other research [12].

To realize the high-frequency oscillation, a transmission mechanism similar to other fast-swimming robotic fishes [16] is applied (Fig. 1(c)). An eccentric shaft is connected from the output shaft of the BLDC motor to the slideway and converts the continuous rotation of the motor in one direction into a fish-like tail beating motion. The slideway is connected to the tail skeleton via a passive revolute joint, which minimizes friction and prevents deadlocks. In this work, it is assumed that the motor rotates at a constant angular velocity and the tail-beating amplitude is designed to be $40°$ as a biologically inspired, large-amplitude motion representative of the vigorous tail oscillation observed during flying fish taxiing, while remaining within a mechanically reliable operating range for the robotic prototype. The caudal fin attached to the tail captures the asymmetrical characteristic, with the lower lobe being elongated, which has been hypothesized to generate greater thrust during taxiing [2]. The caudal fin gradually tapers from its leading edge to its rear, making it more closely resemble that of a real fish.

The tail-pitching structure (Fig. 1(d)) is located between the rigid head and the self-propelled tail. A linear actuator (PQ12-63-6-R, Actuonix) is hinged to a slider that can freely move up and down. The tail is aligned with the head when the linear actuator is fully retracted. When the linear actuator is extracted, it will push the tail, pitching it downwards. The maximum pitching angle is $45°$. A pair of pelvic fins is arranged on two sides of the tail-pitching structure to stabilize the robotic fish [10].

Based on the design, a prototype of the robotic flying fish (Fig. 1(e-h)) is developed with a length of 37.7 cm and a weight of 597 g (547 g without pectoral fins mounted). The selection of materials was guided by a comprehensive evaluation of their waterproofing, toughness, and lightweight attributes.

The head was 3D printed with ultraviolet-curable resin (Clear Resin v5, Formlabs) using a desktop stereolithography (SLA) printer (Form 4, Formlabs) for optimal waterproofing. The rear-end cap was fixed with the streamlined shell by

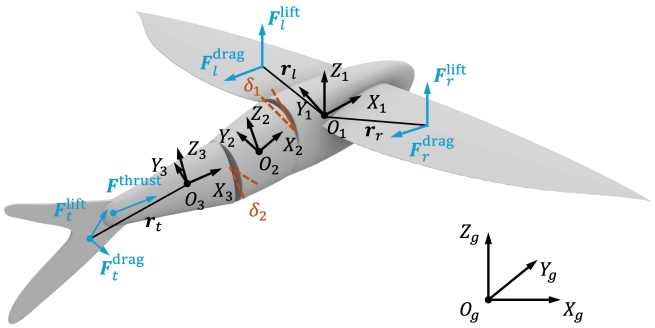

Fig. 2. Schematic illustration depicting the links and coordinate frames of the robotic flying fish. The hydro/aero-dynamic centers of the caudal and pectoral fins are indicated.

screws, and a silicone O-ring (OD: 62 mm, ID: 58 mm) was inserted to ensure waterproofing. The other structural parts were 3D printed by a desktop 3D printer (X1C, Bambu Lab). The tail-pitching structure and the actuation system were printed with a metallic textured polylactic acid (PLA Metal, Bambu Lab) to enhance impact strength. The two structures, including the passive hinge joints, were printed in a single piece to minimize the assembly effort. The caudal fin was made of thermoplastic polyurethane (TPU) with a Shore hardness of 95A (TPU 95A HF, Bambu Lab). Certain flexibility in the caudal fin has been found to generate greater thrust compared with a rigid fin under the same beating frequency [13]. The pectoral fins were made of a foaming polylactic acid (PLA Aero, Bambu Lab) to reduce weight and enhance toughness. Weight distribution was tuned experimentally by adding weights inside the rigid head and foam outside so that the robot achieved near-neutral buoyancy and an approximately level initial head posture at rest.

A microcontroller board (XIAO ESP32S3 Sense, Seeed Studio) with a built-in Wi-Fi module controlled the robot via Wi-Fi commands. The speed command of the BLDC motor was subsequently transmitted to an electronic speed control module (Basic ESC, Blue Robotics), while the position command of the linear motor was directly sent to it. The robot was powered by a three-cell lithium-polymer battery with a maximum charged voltage of 12.6V (3S 850 mAh 100C LiPo-Battery, Zeee). The linear motor is powered by a 5V voltage, which is obtained by stepping down the voltage from the LiPo battery using a voltage converter (MPM3610 5V Buck Converter, Adafruit). All the electronics except the microcontroller were stored in the rigid head.

III. Dynamic Modeling of Robotic Flying Fish

A dynamic model was established to analyze the taxiing locomotion of the robotic flying fish. A Newton-Euler approach was applied to analyze the dynamic model [17].

A. Kinematic analysis

The model and coordinate frames are shown in Fig. 2. To simplify the model, the designed unactuated pelvic fins are neglected, and the caudal fin is assumed to be rigid. For simplicity, the caudal fin is modeled as rigid, and the pelvic fins are neglected. The robotic flying fish is then modeled as three rigid links, connected by two actuated revolute joints. The earth-fixed inertial frame is defined as $O_g - X_gY_gZ_g$ in which the plane $X_gO_gY_g$ is the water surface. The link coordinate frames are defined as $O_i - X_iY_iZ_i$ $(i = 1, 2, 3)$. The origin O_i coincides with the center of mass (COM) of link $\mathcal{L}_i$. The X_i-axis coincides with the longitudinal axis and directs to the anterior, and the Z_i-axis is along the height direction and points toward the dorsum. We define $\boldsymbol{l}_i^{\text{ant}}$ $(i = 2, 3)$ and $\boldsymbol{l}_i^{\text{post}}$ $(i = 1, 2)$ as the vector in the local frame from O_i to the anterior and posterior joint, respectively.

The system takes the tail-pitching angle $\delta_1(t)$ and the tail-beating angle $\delta_2(t)$ as input, which correspond to the linear-motor-driven tail-pitching structure and BLDC-motor-driven propulsion system in the robot design, respectively. Since the three links are rigidly connected, the state of the robot can be fully determined by the state of $\mathcal{L}_1$, namely $\mathbf{x} = (\boldsymbol{x}_1, \dot{\boldsymbol{x}}_1, \ddot{\boldsymbol{x}}_1, \boldsymbol{R}_1, \boldsymbol{\omega}_1, \dot{\boldsymbol{\omega}}_1)$, where $\boldsymbol{x}_1$ is the position of O_1 in the world frame, $\boldsymbol{R}_1 \in SO(3)$ is the rotation matrix from $O_1 - X_1Y_1Z_1$ to the world coordinate, and $\boldsymbol{\omega}_1$ is the vector of angular velocity of $\mathcal{L}_1$.

The rotation matrices of the other two links are obtained from $\boldsymbol{R}_1$, δ_1, and δ_2:

$$\boldsymbol{R}_2 = \boldsymbol{R}_1\boldsymbol{R}_y(\delta_1), \quad \boldsymbol{R}_3 = \boldsymbol{R}_2\boldsymbol{R}_z(\delta_2), \tag{1}$$

where

$$\boldsymbol{R}_y(\delta) = \begin{bmatrix} \cos\delta & 0 & \sin\delta \\ 0 & 1 & 0 \\ -\sin\delta & 0 & \cos\delta \end{bmatrix}, \ \boldsymbol{R}_z(\delta) = \begin{bmatrix} \cos\delta & -\sin\delta & 0 \\ \sin\delta & \cos\delta & 0 \\ 0 & 0 & 1 \end{bmatrix}. \tag{2}$$

The vectors of angular velocities and accelerations of $\mathcal{L}_2$ and $\mathcal{L}_3$ are obtained from $\boldsymbol{\omega}_1$ and $\dot{\boldsymbol{\omega}}_1$:

$$\boldsymbol{\omega}_2 = \boldsymbol{\omega}_1 + \dot{\delta}_1\hat{\boldsymbol{y}}_1, \qquad \boldsymbol{\omega}_3 = \boldsymbol{\omega}_2 + \dot{\delta}_2\hat{\boldsymbol{z}}_2, \tag{3}$$

$$\dot{\boldsymbol{\omega}}_2 = \dot{\boldsymbol{\omega}}_1 + \boldsymbol{\eta}_2, \qquad \dot{\boldsymbol{\omega}}_3 = \dot{\boldsymbol{\omega}}_1 + \boldsymbol{\eta}_3, \tag{4}$$

with

$$\boldsymbol{\eta}_2 = \ddot{\delta}_1\hat{\boldsymbol{y}}_1 + \dot{\delta}_1\left(\boldsymbol{\omega}_1 \times \hat{\boldsymbol{y}}_1\right), \tag{5}$$

$$\boldsymbol{\eta}_3 = \boldsymbol{\eta}_2 + \ddot{\delta}_2\hat{\boldsymbol{z}}_2 + \dot{\delta}_2\left(\boldsymbol{\omega}_2 \times \hat{\boldsymbol{z}}_2\right), \tag{6}$$

where $\hat{\boldsymbol{y}}_1 = \boldsymbol{R}_1\hat{\boldsymbol{e}}_y$, $\hat{\boldsymbol{z}}_2 = \boldsymbol{R}_2\hat{\boldsymbol{e}}_z$, and $\hat{\boldsymbol{e}}_y = \begin{bmatrix} 0 & 1 & 0 \end{bmatrix}^\top$, $\hat{\boldsymbol{e}}_z = \begin{bmatrix} 0 & 0 & 1 \end{bmatrix}^\top$.

The positions of O_2 and O_3 in the world frame are:

$$\boldsymbol{x}_2 = \boldsymbol{x}_1 + \boldsymbol{R}_1\boldsymbol{l}_1^{\text{post}} - \boldsymbol{R}_2\boldsymbol{l}_2^{\text{ant}}, \quad \boldsymbol{x}_3 = \boldsymbol{x}_2 + \boldsymbol{R}_2\boldsymbol{l}_2^{\text{post}} - \boldsymbol{R}_3\boldsymbol{l}_3^{\text{ant}}, \tag{7}$$

The translational velocities at O_2 and O_3 in the world frame are thus calculated as:

$$\dot{\boldsymbol{x}}_i = \dot{\boldsymbol{x}}_{i-1} + \boldsymbol{\omega}_{i-1} \times \left(\boldsymbol{R}_{i-1}\boldsymbol{l}_{i-1}^{\text{post}}\right) - \boldsymbol{\omega}_i \times \left(\boldsymbol{R}_i\boldsymbol{l}_i^{\text{ant}}\right), \ i = 2, 3. \tag{8}$$

The translational accelerations at O_2 and O_3 are formulated in the form of:

$$\ddot{\boldsymbol{x}}_i = \ddot{\boldsymbol{x}}_1 + \boldsymbol{U}_i\dot{\boldsymbol{\omega}}_1 + \boldsymbol{\xi}_i, \ i = 2, 3, \tag{9}$$

with

$$\boldsymbol{U}_2 = -\left[\boldsymbol{R}_1\boldsymbol{l}_1^{\text{post}}\right]_\times + \left[\boldsymbol{R}_2\boldsymbol{l}_2^{\text{ant}}\right]_\times, \tag{10}$$

$$\boldsymbol{U}_3 = \boldsymbol{U}_2 - \left[\boldsymbol{R}_2\boldsymbol{l}_2^{\text{post}}\right]_\times + \left[\boldsymbol{R}_3\boldsymbol{l}_3^{\text{ant}}\right]_\times, \tag{11}$$

$$\begin{aligned}\boldsymbol{\xi}_2 = {} & \boldsymbol{\omega}_1 \times \left(\boldsymbol{\omega}_1 \times \left(\boldsymbol{R}_1\boldsymbol{l}_1^{\text{post}}\right)\right) - \boldsymbol{\eta}_2 \times \left(\boldsymbol{R}_2\boldsymbol{l}_2^{\text{ant}}\right) \\ & - \boldsymbol{\omega}_2 \times \left(\boldsymbol{\omega}_2 \times \left(\boldsymbol{R}_2\boldsymbol{l}_2^{\text{ant}}\right)\right),\end{aligned} \tag{12}$$

$$\begin{aligned}\boldsymbol{\xi}_3 = {} & \boldsymbol{\xi}_2 + \boldsymbol{\eta}_2 \times \left(\boldsymbol{R}_2\boldsymbol{l}_2^{\text{post}}\right) + \boldsymbol{\omega}_2 \times \left(\boldsymbol{\omega}_2 \times \left(\boldsymbol{R}_2\boldsymbol{l}_2^{\text{post}}\right)\right) \\ & - \boldsymbol{\eta}_3 \times \left(\boldsymbol{R}_3\boldsymbol{l}_3^{\text{ant}}\right) - \boldsymbol{\omega}_3 \times \left(\boldsymbol{\omega}_3 \times \left(\boldsymbol{R}_3\boldsymbol{l}_3^{\text{ant}}\right)\right),\end{aligned} \tag{13}$$

where $[\cdot]_\times$ is the skew-symmetric operator.

B. General form of dynamics

The dynamics equation is derived with respect to O_1, i.e., all the forces and moments acting on the other two links are transformed to act on O_1. Then the general matrix form of Newton-Euler's equations of motion is written as:

$$\begin{bmatrix}\boldsymbol{M}_{11} & \boldsymbol{M}_{12} \\ \boldsymbol{M}_{21} & \boldsymbol{M}_{22}\end{bmatrix}\begin{bmatrix}\ddot{\boldsymbol{x}}_1 \\ \dot{\boldsymbol{\omega}}_1\end{bmatrix} = \sum_{i=1}^{3}\boldsymbol{Q}_i^{\text{ext}} + \boldsymbol{Q}^{\text{cent}} + \boldsymbol{Q}^{\text{cons}}, \tag{14}$$

with $\boldsymbol{M}_{11} = \sum_{i=1}^{3}\boldsymbol{M}_i$, $\boldsymbol{M}_{12} = \boldsymbol{M}_2\boldsymbol{U}_2 + \boldsymbol{M}_3\boldsymbol{U}_3$, $\boldsymbol{M}_{21} = \sum_{i=2}^{3}\left[\boldsymbol{x}_i - \boldsymbol{x}_1\right]_\times \boldsymbol{M}_i$, and $\boldsymbol{M}_{22} = \sum_{i=1}^{3}\boldsymbol{I}_i + \sum_{i=2}^{3}\left[\boldsymbol{x}_i - \boldsymbol{x}_1\right]_\times \boldsymbol{M}_i\boldsymbol{U}_i$, where $\boldsymbol{M}_i = m_i\mathbf{I}_{3\times3} + \boldsymbol{R}_i\boldsymbol{M}_i^{\text{add}}\boldsymbol{R}_i^\top$ and $\boldsymbol{I}_i = \boldsymbol{R}_i\left(\boldsymbol{I}_i^{\text{body}} + \boldsymbol{I}_i^{\text{add}}\right)\boldsymbol{R}_i^\top$ $(i = 1, 2, 3)$ are the matrices of mass and moment of inertia of each link involving the added mass terms, denoted by the superscript $^{\text{add}}$. $\boldsymbol{Q}_i^{\text{ext}}$ is the generalized external forces acting on $\mathcal{L}_i$ about O_1. $\boldsymbol{Q}^{\text{cent}}$ and $\boldsymbol{Q}^{\text{cons}}$ are the generalized centrifugal and constraint forces:

$$\boldsymbol{Q}^{\text{cent}} = \begin{bmatrix}\mathbf{0} & -\sum_{i=1}^{3}\boldsymbol{\omega}_i \times \left(\boldsymbol{I}_i\boldsymbol{\omega}_i\right)\end{bmatrix}^\top, \tag{15}$$

$$\boldsymbol{Q}^{\text{cons}} = \sum_{i=2}^{3}\begin{bmatrix}-\boldsymbol{M}_i\boldsymbol{\xi}_i & -\boldsymbol{I}_i\boldsymbol{\eta}_i - \left[\boldsymbol{x}_i - \boldsymbol{x}_1\right]_\times \boldsymbol{M}_i\boldsymbol{\xi}_i\end{bmatrix}^\top. \tag{16}$$

C. Hydrodynamic analysis

In the taxiing locomotion, the flying fish is partially submerged. Such cross-domain locomotion is extremely complicated to model. For simplicity, the fluid where the robotic fish swims is assumed to be inviscid, incompressible, and irrotational. The cross-sections of the body are approximated to be oval with semi-axes $a(s)$ in the y-direction and $b(s)$ in the z-direction, where s denotes the distance from the nose. We proposed a method for analyzing the hydrodynamics of partially submerged bodies based on their submerged geometry. This method extends the hydrodynamic analysis applied in freely-swimming robotic fish. [18].

1) Submerged geometry: Given a cross-section at distance s from the nose, the oval boundary points Ω_s in its local frame $O_i - X_iY_iZ_i$ can be described as $\boldsymbol{r}_{\Omega_s}^{(i)} = \begin{bmatrix}x_{s,i} & a(s)\cos\theta_s & b(s)\sin\theta_s\end{bmatrix}^\top$, where $x_{s,i}$ is the signed distance from O_i to the section centroid. The global position of a point on the oval boundary is $\boldsymbol{r}_{\Omega_s} = \boldsymbol{x}_i + \boldsymbol{R}_i\boldsymbol{r}_{\Omega_s}^{(i)}$. We define the submerged arc of Ω_s as the continuous segment(s) of θ_s where $\boldsymbol{r}_{\Omega_s}\cdot\hat{\boldsymbol{e}}_z < 0$, i.e., $\Omega_s^{\text{sub}} = \{\theta_s \in [0, 2\pi) : \boldsymbol{r}_{\Omega_s}\cdot\hat{\boldsymbol{e}}_z < 0\}$. Then the wetted perimeter of this cross-section is $p_s^{\text{wet}} = \int_{\theta\in\Omega_s^{\text{sub}}}\left\|\frac{\mathrm{d}\boldsymbol{r}_{\Omega_s}^{(i)}}{\mathrm{d}\theta}\right\|\mathrm{d}\theta$.

To compute the submerged area and centroid, we define the following intermediate variables: $c_w = \hat{\boldsymbol{e}}_z^\top\left(\boldsymbol{x}_i + x_{s,i}\boldsymbol{R}_i\hat{\boldsymbol{x}}_i\right)$, $a_w = \hat{\boldsymbol{e}}_z^\top\boldsymbol{R}_i\hat{\boldsymbol{e}}_y$, $b_w = \hat{\boldsymbol{e}}_z^\top\boldsymbol{R}_i\hat{\boldsymbol{e}}_z$; $s_w = a(s)a_w$, $t_w = b(s)b_w$, $m_w = \sqrt{s_w^2 + t_w^2}$, $h_w = -\frac{c_w}{m_w}$, $\boldsymbol{d}_w = \frac{1}{m_w}\begin{bmatrix}a(s)s_w & b(s)t_w\end{bmatrix}^\top$. Then the submerged area is calculated as

$$A_s^{\text{sub}} = \begin{cases}0, & h_w \le -1 \\ \pi a(s)b(s), & h_w \ge 1 \\ a(s)b(s)\bar{A}_s^{\text{sub}}, & -1 < h_w < 1\end{cases}, \tag{17}$$

where $\bar{A}_s^{\text{sub}} = \pi - \arccos h_w + h_w\sqrt{1 - h_w^2}$. And the submerged centroid is

$$\boldsymbol{r}_s^{\text{sub}} = \boldsymbol{x}_i + \boldsymbol{R}_i\begin{cases}x_{s,i}\hat{\boldsymbol{x}}_i, & h_w \ge 1 \\ \begin{bmatrix}x_{s,i} & -\frac{2(1-h_w^2)^{3/2}}{3\bar{A}_s^{\text{sub}}}\boldsymbol{d}_w^\top\end{bmatrix}^\top, & -1 < h_w < 1\end{cases}. \tag{18}$$

The relative incoming flow at the submerged centroid is $\boldsymbol{v}_s^{\text{rel}} = \dot{\boldsymbol{x}}_i + \boldsymbol{\omega}_i \times \left(\boldsymbol{r}_s^{\text{sub}} - \boldsymbol{x}_i\right) - \boldsymbol{v}_{\text{water}}$, where $\boldsymbol{v}_{\text{water}}$ is the velocity of the fluid field.

2) Added mass: In a submerged environment, added mass is the mass of the displaced fluid around the object. For a partially submerged cross-section at a distance of s from the nose, we define the wet fraction as $\beta^{\text{wet}}(s) = \frac{\left|\Omega_s^{\text{sub}}\right|}{2\pi}$. Then the added mass and moment of inertia matrix in the local frame is approximated with a slender body with oval cross-sections [19]:

$$\boldsymbol{M}_i^{\text{add}} = \int \operatorname{diag}\left(0,\ m_{yy}(s),\ m_{zz}(s)\right)\mathrm{d}s, \tag{19}$$

$$\boldsymbol{I}_i^{\text{add}} = \int \operatorname{diag}\left(I_{xx}(s),\ I_{yy}(s),\ I_{zz}(s)\right)\mathrm{d}s, \tag{20}$$

with $m_{yy}(s) = \beta^{\text{wet}}(s)\rho_{\text{w}}\pi b^2(s)$, $m_{zz}(s) = \beta^{\text{wet}}(s)\rho_{\text{w}}\pi a^2(s)$, $I_{xx}(s) = \beta^{\text{wet}}(s)\rho_{\text{w}}\left(a^2(s) - b^2(s)\right)^2$, $I_{yy}(s) = m_{zz}(s)x_{s,i}^2$, $I_{zz}(s) = m_{yy}(s)x_{s,i}^2$, where ρ_{w} is the density of water.

3) Hydrodynamic forces on the body: The hydrodynamic drag and buoyancy on the body are considered. For a cross-section at a distance of s from the nose, its buoyancy is calculated as $\mathrm{d}\boldsymbol{F}_s^{\text{buoy}} = \rho_{\text{w}}gA_s^{\text{sub}}\hat{\boldsymbol{e}}_z$ and $\mathrm{d}\boldsymbol{\tau}_s^{\text{buoy}} = (\boldsymbol{r}_s^{\text{sub}} - \boldsymbol{r}_i)\times\mathrm{d}\boldsymbol{F}_s^{\text{buoy}}$.

The drag force comes from the pressure difference and friction viscosity and is formalized as [17]:

$$\begin{aligned}\mathrm{d}\boldsymbol{F}_s^{\text{drag}} = -\frac{1}{2}\rho_{\text{w}}\Big(& C_i^{\text{fric}}p_s^{\text{wet}}\left(\boldsymbol{v}_s^{\text{rel}}\cdot\hat{\boldsymbol{x}}_i\right)^2\hat{\boldsymbol{x}}_i \\ & + C_i^{\text{drag}}h_s^{\text{wet}}\left(\boldsymbol{v}_s^{\text{rel}}\cdot\hat{\boldsymbol{y}}_i\right)^2\hat{\boldsymbol{y}}_i\Big)\mathrm{d}s,\end{aligned} \tag{21}$$

$$\mathrm{d}\boldsymbol{\tau}_s^{\text{drag}} = \left(\boldsymbol{r}_s^{\text{sub}} - \boldsymbol{r}_i\right)\times\mathrm{d}\boldsymbol{F}_s^{\text{drag}}. \tag{22}$$

with $h_s^{\text{wet}} = \int_{\theta\in\Omega_s^{\text{sub}}}\left|\hat{\boldsymbol{v}}_s^{\text{rel}}\cdot\boldsymbol{t}_s(\theta)\right|\mathrm{d}\theta$ as the projected area, where $\boldsymbol{t}_s(\theta) = \boldsymbol{R}_i\cdot\begin{bmatrix}0 & -a(s)\sin\theta & b(s)\cos\theta\end{bmatrix}^\top$, and C_i^{fric} and C_i^{drag} are the dimensionless friction and drag coefficients

to denote the damping effects of fluid, respectively. The generalized drag force exerted on $\mathcal{L}_i$ is

$$\boldsymbol{Q}_i^{\text{hydro}} = \int_i \begin{bmatrix} \mathrm{d}\boldsymbol{F}_s^{\text{drag}} \\ \mathrm{d}\boldsymbol{\tau}_s^{\text{drag}} + (\boldsymbol{x}_i - \boldsymbol{x}_1) \times \mathrm{d}\boldsymbol{F}_s^{\text{drag}} \end{bmatrix}. \tag{23}$$

The Lighthill's large-amplitude-elongated-body theory [20] is applied to obtain the thrust generated by the fish's undulating body. The thrust force acting at the peduncle is calculated by

$$\boldsymbol{F}^{\text{thrust}} = \frac{1}{2} m_a v_y^2 \hat{\boldsymbol{x}}_3 + m_a v_x v_y \hat{\boldsymbol{y}}_3, \tag{24}$$

with $m_a = \frac{1}{4}\rho_{\text{w}} \pi d^2$ being the added mass at the peduncle, where d is the immersed depth at the peduncle. v_x and v_y are the $x-$ and $y-$components of the speed at the peduncle in the local frame of $\mathcal{L}_3$. The generalized thrust force is then formalized as:

$$\boldsymbol{Q}^{\text{thrust}} = \begin{bmatrix} \boldsymbol{F}^{\text{thrust}} & \left(\boldsymbol{l}_3^{\text{post}} + \boldsymbol{x}_3 - \boldsymbol{x}_1\right) \times \boldsymbol{F}^{\text{thrust}} \end{bmatrix}^\top. \tag{25}$$

4) Hydrodynamic forces on the caudal fin: The lift-drag model [21] is employed to calculate hydrodynamic forces exerted on the caudal fin. Given the asymmetric caudal fin of the flying fish, characterized by a larger lower lobe, the vertical position of the hydrodynamic center is approximately aligned with the geometric center. Conversely, the horizontal position is estimated to be situated at a quarter of the mean chord length, denoted as $c_t = \frac{A_t}{b_t}$, where A_t represents the area of the fin and b_t signifies the span from the tip to the base of the fin. We then denote O_t as the hydrodynamic center of the caudal fin and $\boldsymbol{r}_t^{(3)}$ as the constant body-fixed vector from O_3 to O_t.

The lift and drag forces are calculated as follows:

$$\Psi_t = \frac{1}{2}\rho_{\text{w}} \left\|\boldsymbol{v}_t^{\text{rel}}\right\|^2 A_t C_t^{\Psi}(\alpha_t), \quad \Psi \in \{L, D\}, \tag{26}$$

where $\boldsymbol{v}_t^{\text{rel}} = \dot{\boldsymbol{x}}_3 + \boldsymbol{\omega}_3 \times \left(\boldsymbol{R}_3 \boldsymbol{r}_t^{(3)}\right)$ is the velocity at the hydrodynamic center relative to the fluid field in the world coordinate, $\alpha_t = \arcsin\left(\hat{\boldsymbol{y}}_3 \cdot \hat{\boldsymbol{v}}_t^{\text{rel}}\right)$ is the angle of attack (AoA), C_t^L and C_t^D are the lift and drag coefficients related to the AoA respectively. The three-dimensional lift and drag forces exerted on the caudal fin are:

$$\boldsymbol{F}_t^{\text{lift}} = L_t \cdot \frac{\boldsymbol{v}_t^{\text{rel}} \sin\alpha_t - \operatorname{sgn}\left(\hat{\boldsymbol{n}}_t \cdot \hat{\boldsymbol{v}}_t^{\text{rel}}\right)\hat{\boldsymbol{n}}_t}{\left\|\boldsymbol{v}_t^{\text{rel}} \sin\alpha_t - \operatorname{sgn}\left(\hat{\boldsymbol{n}}_t \cdot \hat{\boldsymbol{v}}_t^{\text{rel}}\right)\hat{\boldsymbol{n}}_t\right\|}, \tag{27}$$

$$\boldsymbol{F}_t^{\text{drag}} = -D_t \hat{\boldsymbol{v}}_t^{\text{rel}}. \tag{28}$$

Then the tail-generated generalized force is

$$\boldsymbol{Q}^{\text{fin}} = \begin{bmatrix} \boldsymbol{F}_t^{\text{drag}} + \boldsymbol{F}_t^{\text{lift}} \\ \left(\boldsymbol{R}_3 \boldsymbol{r}_t^{(3)} + \boldsymbol{x}_3 - \boldsymbol{x}_1\right) \times \left(\boldsymbol{F}_t^{\text{drag}} + \boldsymbol{F}_t^{\text{lift}}\right) \end{bmatrix}. \tag{29}$$

D. Aerodynamic analysis

For the aerodynamics of the flying fish, we only consider the aerodynamic forces exerted on the pectoral fins. For the submerged body, the aerodynamic forces are negligible compared with their hydrodynamic counterparts. For simplicity, the aerodynamic centers are located at the COMs of the fins.

TABLE I
PHYSICAL MODEL PARAMETERS

Parameters	Units	$\mathcal{L}_1$	$\mathcal{L}_2$	$\mathcal{L}_3$
m_i	g	262.3	176.3	158.4
$I_i(\text{xx}, \text{yy}, \text{zz})$	kg.m^2	1.6, 7.7, 7.4	9.2, 1.2, 1.0	1.1, 0.4, 0.4
l_i^{ant}	mm	122	32	55
l_i^{post}	mm	78	37	53
A_{wing}	mm^2	24271	-	-
A_t	mm^2	-	-	4900

The lift and drag forces exerted on the left pectoral fin are computed as [12]:

$$\boldsymbol{F}_l^{\text{lift}} = \frac{1}{2}\rho_{\text{a}} \|\boldsymbol{V}_\infty\|^2 A_{\text{wing}} C_l^{\text{lift}}(\alpha_l) \hat{\boldsymbol{z}}_1, \tag{30}$$

$$\boldsymbol{F}_l^{\text{drag}} = -\frac{1}{2}\rho_{\text{a}} \|\boldsymbol{V}_\infty\|^2 A_{\text{wing}} C_l^{\text{drag}}(\alpha_l) \hat{\boldsymbol{v}}_{l,\parallel}, \tag{31}$$

where $\boldsymbol{V}_\infty = \dot{\boldsymbol{x}}_1 + \boldsymbol{\omega}_1 \times \left(\boldsymbol{R}_1 \boldsymbol{r}_l^{(1)}\right) - \boldsymbol{v}_{\text{wind}}$ is the relative flow seen by the left pectoral fin, $\alpha_l = \arctan\frac{-V_z}{V_x}$ is the AoA, $\hat{\boldsymbol{v}}_{l,\parallel} = \frac{V_x \hat{\boldsymbol{x}}_1 + V_z \hat{\boldsymbol{z}}_1}{\sqrt{V_x^2 + V_z^2}}$, A_{wing} is the surface area of the pectoral fin, and ρ_{a} is the air density. The total force is $\boldsymbol{F}_l = \boldsymbol{F}_l^{\text{lift}} + \boldsymbol{F}_l^{\text{drag}}$. Thus, the generalized aerodynamic force is

$$\boldsymbol{Q}^{\text{LW}} = \begin{bmatrix} \boldsymbol{F}_l & \left(\boldsymbol{R}_1 \boldsymbol{r}_l^{(1)}\right) \times \boldsymbol{F}_l \end{bmatrix}^\top. \tag{32}$$

The generalized aerodynamic force contributed by the right pectoral fin $\boldsymbol{Q}^{\text{RW}}$ can be calculated in the same method.

E. Final dynamic model

Based on the analysis of the generalized forces above, the generalized external forces about O_1 can be expressed as:

$$\boldsymbol{Q}_i^{\text{ext}} = \boldsymbol{Q}_i^{\text{g}} + \begin{cases} \boldsymbol{Q}_1^{\text{hydro}} + \boldsymbol{Q}^{\text{LW}} + \boldsymbol{Q}^{\text{RW}}, & i = 1 \\ \boldsymbol{Q}_2^{\text{hydro}}, & i = 2 \\ \boldsymbol{Q}_3^{\text{hydro}} + \boldsymbol{Q}^{\text{thrust}} + \boldsymbol{Q}^{\text{fin}}, & i = 3 \end{cases}, \tag{33}$$

where $\boldsymbol{Q}_i^{\text{g}} = \begin{bmatrix} -m_i g \hat{\boldsymbol{e}}_z & -(\boldsymbol{x}_i - \boldsymbol{x}_1) \times m_i g \hat{\boldsymbol{e}}_z \end{bmatrix}^\top$ is the generalized gravity force of $\mathcal{L}_i$.

The model parameters, including the mass, dimensions, and moment of inertia of the robotic flying fish, were determined from the developed prototype, listed in Table I. The hydrodynamic parameters were approximated from those in other robotic fish research papers [18], [21], and the aerodynamic parameters were derived from previous studies on flying fish [6], [7], [10]. Consequently, C_i^{fric} and C_d^{fric} were uniformly set to be 0.1 and 2 on all the links, respectively. The hydrodynamic parameters on the caudal fin were set to $C_t^L(\alpha) = 1.83|\alpha|$ and $C_t^D(\alpha) = 0.98|\alpha|^2 + 0.35|\alpha| + 0.04$. The aerodynamic parameters on the pectoral fins were set to $C_{l/r}^{\text{lift}}(\alpha) = 3.06\alpha - 0.05$ and $C_{l/r}^{\text{drag}}(\alpha) = 2.77\alpha^2 - 0.07\alpha + 0.06$. To simplify the hydro/aero-dynamics analysis, the generalized forces at the peduncle and caudal fin were only considered when the corresponding hydrodynamic centers were submerged beneath the water's surface. Conversely, the generalized forces at the pectoral fins were only considered when the aerodynamic centers were positioned above the water's surface.

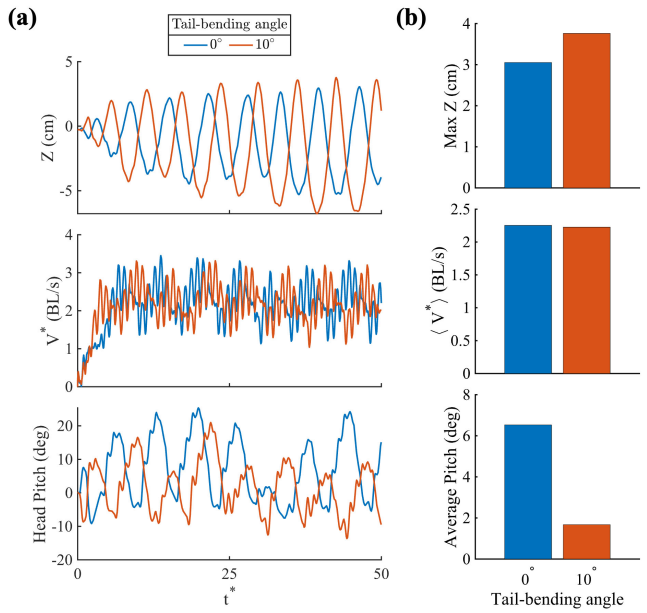

Fig. 3. Data plots of the dynamic simulations of the flying fish taxiing locomotion. The flying fish was simulated for 5 s with a driving frequency of 10 Hz. (a) Plots of the height above water Z, velocity V^* at O_1, and the head pitch over time. (b) Comparison of the maximum height, average velocity, and average head pitch for the flying fish taxiing without tail-pitching and with a 10° tail-pitching.

IV. Results and Discussions

In this section, we simulated the taxiing locomotion of flying fish and tested the performance of the developed robotic flying fish. In this study, time is non-dimensionalized as $t^* = tf$, where f is the tail-beating frequency.

A. Simulation of the flying fish taxiing

The taxiing locomotion of the flying fish was investigated using the proposed cross-domain dynamics. The flying fish was simulated from rest, with its head ($\mathcal{L}_1$) parallel to the water surface and its body partially submerged to achieve neutral buoyancy. The pectoral fins were supposed to be deployed when they were above water. The tail was set to beat following the function $\delta_2 = \arcsin(A_2 \sin(2\pi f t))$, where $A_2 = 20°$ and $f = 10$ Hz. The function aligns with the designed transmission structure on the physical robot. The tail-pitching angle δ_1 was set to 0° and 10°. The trajectories and orientations were recorded at O_1, as shown in Fig. 3(c). Accordingly, the height above water refers to the vertical position of O_1.

A comparison between the average forward velocity, average head pitch, and the maximum height was demonstrated for the flying fish with and without tail-pitching, as illustrated in Fig. 3(d). The results demonstrate that when the tail was pitched downward, the average velocity decreased by 1.2%, and the average head pitch decreased by 74.3%. The decrease in the average head pitch was primarily attributed to an increased moment generated by the upward component of the thrust force, which resulted in a downward rotation of the head.

The flying fish has been observed to break through the water surface in the simulations. With a tail pitching of

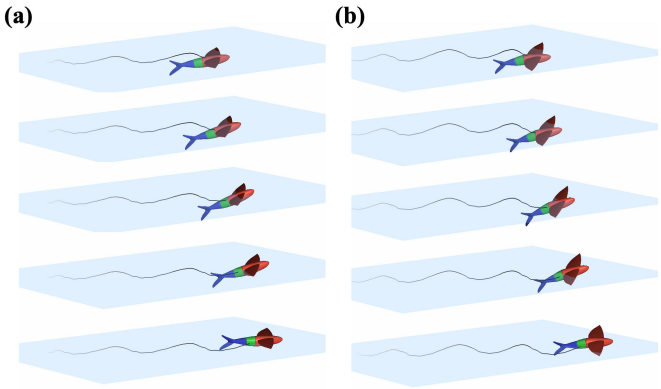

Fig. 4. Animation of the flying fish without tail-pitching (a) and with a 10° tail-pitching (b). Four cycles were captured before the flying fish reached a peak height above water. The translucent blue plane represents the water surface. The spatial trajectories at O_1 are plotted, where time increases as the color deepens from light to dark.

10°, the peak height above the water was recorded to be 23.2% higher, reaching 3.76 cm. By capturing the four cycles preceding its peak height in both configurations (Fig. 4), it is further observed that in the tail-pitching case, the flying fish leaped through the water at an AoA of 18.2°. Upon reaching the peak height, the AoA decreased to 5.0°. In contrast, the flying fish leaped through the water at an AoA of 22.3°, and the AoA decreased to 3.6° upon reaching the peak height in the other configuration. Consequently, the tail-pitching configuration reduces the rate of AoA drop, maintaining the body at a larger AoA throughout the leaping process. The larger angle of attack indicates an increase in the lift force. Previous wind tunnel studies have measured a maximum lift-to-drag ratio of the pectoral fins at an AoA between 5 and 10 degrees [7], [10]. With the tail-pitching, the AoA of the flying fish in our simulation predominantly fell within this range, suggesting a high aerodynamic efficiency. These metrics are directly relevant to transition performance during taxiing: a higher peak height indicates greater body emergence from the water surface, while a more favorable AoA range suggests improved aerodynamic conditions during the water-to-air transition. Together, they provide quantitative evidence that tail pitching improves transition readiness.

B. Thrust force tests

The thrust forces of the robot in the forward (x) and upward (z) directions were measured in a fixed condition, as illustrated in Fig. 5(a). A load cell (F/T Sensor Gamma 16016, ATI Industrial Automation) was used as the force sensor. The tail-pitching and tail-beating structures of the robot were attached to a rod (Fig. 5(b)). When the robot generated a thrust, the force was directly applied to the force sensor. The output signal of the load cell was recorded using an Ethernet box (9105-NETB, ATI Industrial Automation) controlled by a Python code and saved on a computer. The sampling rate was set at 500 Hz. The force sensor was tared to zero before each test. Subsequently, the robot was then driven for 10 s at a 10 Hz beating frequency. The average of the recorded sensor output over 2 s was calculated to be the thrust force.

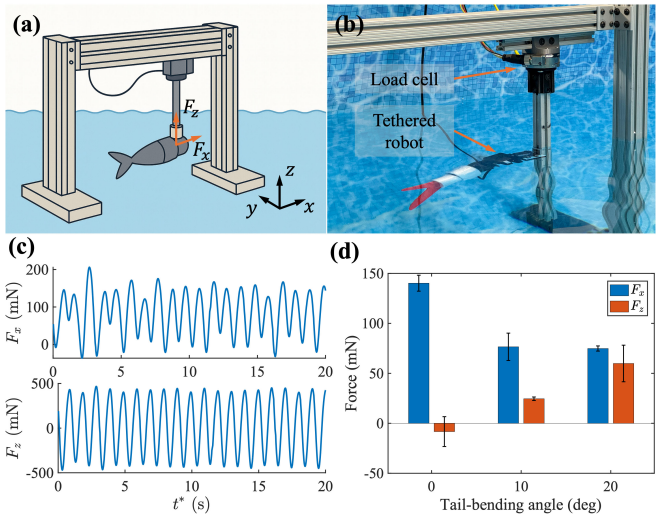

Fig. 5. Thrust force tests. (a) Illustration of the experimental setup for the thrust force tests. (b) The tethered robot is mounted to the load cell. (c) Plots of the forward (F_x) and upward (F_z) forces measured within 2 s (20 cycles), with a tail-pitching angle of 10°. (d) Forward and upward forces measured with different tail-pitching angles.

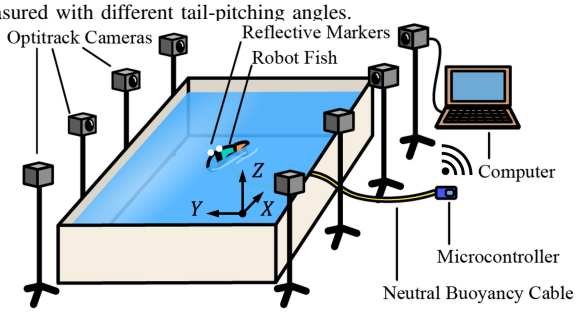

Fig. 6. Experimental setup of the free-swimming tests. Eight Optitrack motion tracking cameras were placed around a 5 m × 2 m pool. Reflective markers were mounted on the robot fish to track the positions. The microcontroller sent motor signals to the robot through a neutral buoyancy cable (Fathom ROV Tether, Blue Robotics). Despite potential drag and disturbance, the same tether configuration was used across all tests, ensuring the validity of the reported comparative trends. The microcontroller and motion tracking system are connected to a computer via Wi-Fi and Ethernet, respectively.

The thrust forces were measured at tail-pitching angles of 0°, 10°, and 20°, each for three repetitions. Both forward and upward forces exhibit wave-like patterns over time. However, the forward force remains predominantly positive, while the upward force exhibits greater amplitude with positive and negative phases each occupying approximately half of each cycle (Fig. 5(c)). It has been observed that as the tail-pitching angles increased, despite a falloff in the forward thrust force, the tail-beating motion provided a larger upward force, which explained the decrease in swimming velocity and head pitch observed in the simulation. At a tail-pitching angle of 20°, the thrust force generated an upward force of 0.6 N, exceeding 10% of the total weight (Fig. 5(d)). This indicates that the tail-pitching strategy introduces additional lift force on the flying fish, which is beneficial to its leaping through the water and takeoff.

C. Free-swimming tests

We tested the performance of the robotic flying fish freely swimming in water, without the pectoral fins mounted. The

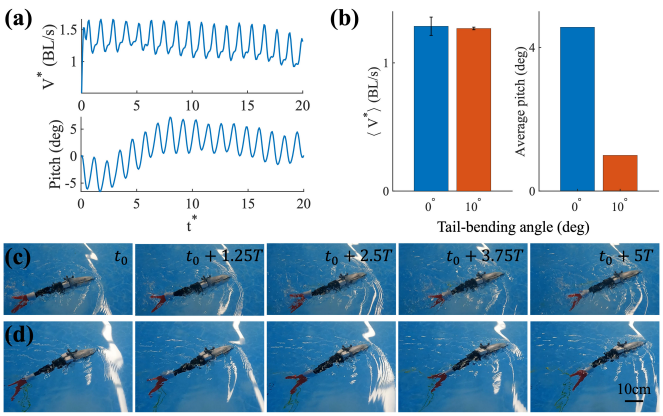

Fig. 7. Free-swimming tests of the robotic flying fish. (a) The experimental setup of the free-swimming tests. Eight OptiTrack PrimeX 13 cameras were positioned around a pool to track the robot's motions. (b) Plots of velocity and head pitch recorded for the robotic fish swimming without tail-pitching. (c) Comparison of the average velocity and peak head pitch with and without tail-pitching. (d, e) Snapshots of five cycles of robotic fish swimming, with (d) and without (c) tail-pitching.

free-swimming tests were carried out in a 5-m-long and 2-m-wide pool (Fig. 6). The forward speed and head pitch angle were measured using a motion tracking system (PrimeX 13, Optitrack). The sampling rate of the system was set to 120 Hz. Simultaneously, a waterproof high-speed camera with a frame rate of 120 fps (Hero9 Black, GoPro) positioned at the edge of the pool captured sequential images of the robot's movements. During preliminary testing, measuring vertical height during free-swimming was challenging because motion-tracking cameras were positioned at similar pool elevations to cover the water surface, and the region near the water surface was not calibrated. Instead of reporting absolute height, we used the waterline position on the rigid head and the measured head pitch angle as qualitative indicators of body elevation relative to the water surface.

The robotic fish was released from rest with its rigid head parallel to the water's surface, resulting in a head pitch angle of zero. The driving frequency of the robot was set at 10 Hz, and the tail-pitching angles were set at 0° and 10°. Each configuration was tested three times. When the tail was not pitched, the robotic fish was measured swimming at an average velocity of 1.33 BL/s. Initially, the head pitched downward during the acceleration phase, but it eventually pitched upward when the fish reached a steady state (Fig. 7(b)). When the tail was pitched by 10°, the average velocity decreased subtly by 4.4% (Fig. 7(c)). Furthermore, the average head pitch angle recorded experienced a significant decrease of 78.2%. These trends are in accordance with the simulation outcomes. The waterline was observed to be slightly above the water surface (Fig. 7(d, e)) in both configurations. Given that the head pitch decreased when the tail was pitched, it can be inferred that the center of mass of the head was further elevated with the tail-pitching mechanism.

V. Conclusions

In this research, we examined the taxiing locomotion of the flying fish using robotic methods, with a particular focus on the impact of the tail-pitching mechanism on its performance. We developed a robotic flying fish prototype with a tail-pitching structure. A novel cross-domain dynamics model was then formulated to simulate the free-swimming taxiing locomotion of the flying fish. The thrust forces in the forward and upward directions were measured. The free-swimming tests of the robotic flying fish were performed with physical experiments and dynamic simulations. The performance of robotic flying fish with and without tail-pitching was examined and analyzed. The results demonstrate that when the tail was pitched downward, the tail generated a larger thrust force in the upward direction, and the flying fish gained the ability to leap through the water surface and attain a higher peak height above the water's surface, with only a minimal reduction in speed and a decrease in the average pitch. Moreover, the dynamic simulation results indicate that despite the decrease in average pitch, the flying fish was able to leap above the water with an angle of attack that falls within the range that maximizes aerodynamic efficiency. Therefore, it can be concluded that pitching the tail downward provides extra benefits for the flying fish in taking off, in addition to keeping the caudal fin immersed in water when the body is above water [13]. In this study, transition performance is evaluated using pre-takeoff taxiing metrics, while post-transition metrics such as gliding distance and full takeoff success rate remain to be quantified in future work.

Gaps still exist between the robotic and biological flying fish. The primary cause lies in lower beating frequency and swimming speed compared to real flying fish, which have been documented to reach speeds of up to 10 m/s in water while maintaining a beating frequency between 50 and 70 Hz [2]. Achieving a higher beating frequency presents a challenge to the impact strength of the structure designed for the robotic fish. The present study therefore focuses on one robot size and a 10 Hz operating condition, while frequency and geometric scaling effects remain outside the scope of this work and will be addressed in future work. Furthermore, high-frequency locomotion introduces stability concerns. In both our pool tests and dynamic simulations, evident rolling instability was observed as the tail-pitching angle was further increased. Future research should focus on significantly increasing the beating frequency and swimming speed of both the robotic prototype and the dynamic simulation. Specifically, the robot design should be progressively optimized, enhancing structural strength, reducing weight, and possibly incorporating a direct-driven actuation method to minimize power transmission [22]. The model can be refined by incorporating ground effects that may reduce drag [6] and by calibrating hydrodynamic coefficients through quantitative comparison of predicted and measured cycle-averaged thrust components. Additionally, control strategies should be integrated to ensure the robot's stability. Furthermore, other aspects of taxiing locomotion remain unexplored, such as pectoral fin deployment strategies.

References

[1] K. Low, T. Hu, S. Mohammed, J. Tangorra, and M. Kovac, "Perspectives on biologically inspired hybrid and multi-modal locomotion," *Bioinspiration & biomimetics*, vol. 10, no. 2, p. 020301, 2015.

[2] J. Davenport, "How and why do flying fish fly?" *Reviews in Fish Biology and Fisheries*, vol. 4, no. 2, pp. 184–214, 1994.

[3] C. Breder, "On the structural specilization of flying fishes from the standpoint of aerodynamics," *Copeia*, vol. 1930, no. 4, pp. 114–121, 1930.

[4] K. Möbius, "Flying-fish do not fly," *Nature*, vol. 31, no. 792, pp. 192–192, 1885.

[5] Y. Makiguchi, K. Kuramochi, S. Iwane, T. Kojima, and Y. Naito, "Take-off performance of flying fish cypselurus heterurus doederleini measured with miniature acceleration data loggers," *Aquatic Biology*, vol. 18, no. 2, pp. 105–111, 2013.

[6] H. Park and H. Choi, "Aerodynamic characteristics of flying fish in gliding flight," *Journal of Experimental Biology*, vol. 213, no. 19, pp. 3269–3279, 2010.

[7] J. Deng, L. Zhang, Z. Liu, and X. Mao, "Numerical prediction of aerodynamic performance for a flying fish during gliding flight," *Bioinspiration & biomimetics*, vol. 14, no. 4, p. 046009, 2019.

[8] B. E. Flammang and M. E. Porter, "Bioinspiration: applying mechanical design to experimental biology," *Integrative and Comparative Biology*, vol. 51, no. 1, pp. 128–132, 2011.

[9] A. Gao and A. H. Techet, "Design considerations for a robotic flying fish," in *OCEANS'11 MTS/IEEE KONA*. IEEE, 2011, pp. 1–8.

[10] V. Saro-Cortes, Y. Cui, T. Dufficy, A. Boctor, B. E. Flammang, and A. Wissa, "An adaptable flying fish robotic model for aero-and hydrodynamic experimentation," *Integrative and Comparative Biology*, vol. 62, no. 5, pp. 1202–1216, 2022.

[11] K. Kawachi, Y. Inada, and A. Azuma, "Optimal flight path of flying fish," *Journal of Theoretical Biology*, vol. 163, no. 2, pp. 145–159, 1993.

[12] D. Chen, Z. Wu, H. Dong, Y. Meng, and J. Yu, "Platform development and gliding optimization of a robotic flying fish with morphing pectoral fins," *Bioinspiration & Biomimetics*, vol. 18, no. 3, p. 036010, 2023.

[13] J. Deng, S. Wang, L. Zhang, and X. Mao, "Why does a flying fish taxi on sea surface before take-off? a hydrodynamic interpretation," *bioRxiv*, p. 765560, 2019.

[14] P. R. Bandyopadhyay, "Flying fish sculls to taxi and perturbs wing lift with travelling waves to land," in *Fluids Engineering Division Summer Meeting*, vol. 50282. American Society of Mechanical Engineers, 2016, p. V01AT04A001.

[15] A. L. Thomas and G. K. Taylor, "Animal flight dynamics i. stability in gliding flight," *Journal of theoretical biology*, vol. 212, no. 3, pp. 399–424, 2001.

[16] J. Zhu, C. White, D. K. Wainwright, V. Di Santo, G. V. Lauder, and H. Bart-Smith, "Tuna robotics: A high-frequency experimental platform exploring the performance space of swimming fishes," *Science Robotics*, vol. 4, no. 34, p. eaax4615, 2019.

[17] J. Yu, J. Yuan, Z. Wu, and M. Tan, "Data-driven dynamic modeling for a swimming robotic fish," *IEEE Transactions on industrial electronics*, vol. 63, no. 9, pp. 5632–5640, 2016.

[18] D. Chen, Z. Wu, Y. Meng, M. Tan, and J. Yu, "Development of a high-speed swimming robot with the capability of fish-like leaping," *IEEE/ASME Transactions on Mechatronics*, vol. 27, no. 5, pp. 3579–3589, 2022.

[19] E. V. Lewis, "Principles of naval architecture," *Motions in waves and controllability*, pp. 126–136, 1989.

[20] J. Wang, F. Alequin-Ramos, and X. Tan, "Dynamic modeling of robotic fish and its experimental validation," in *2011 IEEE/RSJ International Conference on Intelligent Robots and Systems*. IEEE, 2011, pp. 588–594.

[21] X. Zheng, M. Xiong, R. Tian, J. Zheng, M. Wang, and G. Xie, "Three-dimensional dynamic modeling and motion analysis of a fin-actuated robot," *IEEE/ASME Transactions on Mechatronics*, vol. 27, no. 4, pp. 1990–1997, 2022.

[22] K. Iguchi, T. Shimooka, S. Uchikai, Y. Konno, H. Tanaka, Y. Ikemoto, and J. Shintake, "Agile robotic fish based on direct drive of continuum body," *npj Robotics*, vol. 2, no. 1, p. 7, 2024.